Materials Advances

ROYAL SOCIETY OF CHEMISTRY

PAPER

View Article Online
View Journal | View Issue

Cite this: *Mater. Adv.*, 2024, 5, 749

2D/2D *Z*-scheme WO_3/g-C_3N_4 heterojunctions for photocatalytic organic pollutant degradation and nitrogen fixation†

Yasi Li [a] and Junkai Wang*[b]

Two-dimensional/two-dimensional (2D/2D) *Z*-scheme WO_3/g-C_3N_4 heterojunctions were successfully prepared by facile rapid calcination, which exhibited considerable photocatalytic performance in environmental application and energy application without any cocatalyst. The synthesized 2D/2D *Z*-scheme WO_3/g-C_3N_4 significantly improved the visible-light photocatalytic degradation of tetracycline hydrochloride (TC-HCl), and 40%WO_3/g-C_3N_4 had the best photocatalytic degradation effect. 40%WO_3/g-C_3N_4 could also degrade rhodamine B (RhB), methylene blue (MB) and methyl orange (MO), and RhB was almost completely degraded after 20 min irradiation. $^{\bullet}O_2^-$ was the main active species in the degradation process of 40%WO_3/g-C_3N_4. The 2D/2D *Z*-scheme heterostructure enhanced the photogenerated electron–hole separation and transfer ability and possessed good photocatalytic stability. The 2D/2D *Z*-scheme WO_3/g-C_3N_4 heterojunction system was first used in nitrogen fixation. 40%WO_3/g-C_3N_4 can simultaneously achieve photocatalytic nitrogen reduction reaction (NRR) and nitrogen oxidation reaction (NOR) to produce NH_4^+ and NO_3^-, respectively, using air as a nitrogen source. However, in the presence of a hole sacrificial agent and N_2 as a nitrogen source, the photocatalytic nitrogen fixation reaction of 40%WO_3/g-C_3N_4 was dominated by NRR. The nitrogen fixation products and their possible mechanisms were also discussed. This study confirms that the designed 2D/2D *Z*-scheme WO_3/g-C_3N_4 heterojunctions have great potential in the photocatalytic degradation of different-type organic pollutants and regulable photocatalytic NRR and NOR reactions.

Received 27th October 2023,
Accepted 4th December 2023

DOI: 10.1039/d3ma00915g

rsc.li/materials-advances

Introduction

Environmental safety and energy resources are among the primary needs for human survival and development. Photocatalysis is regarded as one of the most hopeful methods for environment remediation and energy conversion because of its mild reaction conditions, no secondary pollution, and low energy consumption.[1–4] Under light irradiation, the semiconductor photocatalysts are excited to produce photogenerated carriers, which can directly or indirectly participate in the oxidation–reduction reaction.[1–4] Among the visible-light catalytic materials, WO_3 and g-C_3N_4 photocatalytic materials have the advantages of a suitable energy band structure, good visible-light response range, and relatively simple preparation process.[5–7] Therefore, WO_3 and g-C_3N_4 are ideal materials for constructing efficient visible-light catalysts. Furthermore, if the two materials are integrated to construct type-II or *Z*-scheme heterojunctions, the electrons (e^-) and holes (h^+) can be physically separated, favoring the redox reaction.[19,20] In addition, the *Z*-scheme can simultaneously use the more positive valence band (VB) of one semiconductor and the more negative conduction band (CB) of the other semiconductor, so it has a stronger redox capacity than the one-component semiconductor.[8–16] Two-dimensional/two-dimensional (2D/2D) composite structures have the largest interface contact area, which is conducive to photogenerated carrier transmission.[9–16] Therefore, 2D/2D *Z*-scheme heterojunctions can effectively enhance the performance of WO_3/g-C_3N_4 photocatalysts. The reported 2D/2D *Z*-scheme WO_3/g-C_3N_4 heterojunction systems had complex synthesis, insufficient application research, need for cocatalyst and other deficiencies to some degree.[9–16] Thus, it is necessary to further study the 2D/2D *Z*-scheme WO_3/g-C_3N_4 heterojunction in more ways.

Industrial manufacturing, agricultural production, and daily life produce much wastewater. Organic pollutants in wastewater are toxic, accumulative, and challenging to degrade even at low concentrations, posing a serious threat to the water environment.[17] There are a variety of organic pollutants with

[a] *Department of Mechanical Engineering, College of Engineering, Shantou University, Shantou 515063, China*
[b] *College of Chemistry and Chemical Engineering, Shantou University, Shantou 515063, China. E-mail: jkwang@stu.edu.cn*

† Electronic supplementary information (ESI) available. See DOI: https://doi.org/10.1039/d3ma00915g

various properties in environmental water bodies, such as organic dyes, antibiotics, surfactants, and endocrine disruptors.[17–19] Tetracycline hydrochloride (TC-HCl) has been widely used in humans and animals as an inexpensive broad-spectrum antibiotics.[20–23] TC-HCl easily accumulates in water and soil systems because of its excellent water solubility and long half-life.[20–23] Organic dyes are common organic pollutants, and the same method has different removal effects on dyes with different properties.[24] The traditional removal methods of organic pollutants in the water include physical adsorption, chemical oxidation, and biodegradation. However, most of them have the disadvantages of poor efficiency, complicated methods, high cost, or easily causes secondary pollution.[16,21–23] The degradation of different-type organic pollutants in water is an urgent problem to be solved.

Moreover, nitrogen is an indispensable component of the biological structure.[25–27] It is found in proteins and nucleic acids, and most organisms except nitrogen-fixing microorganisms cannot directly use N_2.[25,28,29] Nitrogen fixation is the conversion of N_2 to simple nitrogenous compounds (nitric oxide, ammonia and others), followed by the generation of more complex compounds that can be used by organisms.[29,30] In recent years, NH_3 has become a crucial raw material and green energy carrier.[28] Nevertheless, the traditional Haber–Bosch process remains the dominant industrial NH_3 production method, which consumes excessive fossil and releases harmful gases.[25,28,30–33] HNO_3 is also a vital raw material in agriculture, military, chemical industry and other areas.[34,35] However, the industrial HNO_3 is synthesized by the Ostwald process through catalytic oxidation of NH_3, so this method is highly energy-consuming.[31,32,34,35] At present, most of the new methods of artificial nitrogen fixation are to reduce N_2 to produce NH_3. However, there are few studies on the oxidation of N_2 to produce HNO_3 or N_2 disproportionation reaction. Therefore, developing eco-friendly and low-cost methods to fix N_2 by directly forming NH_3 and HNO_3 is of great interest.[34,35]

In this paper, 2D/2D *Z*-scheme WO_3/g-C_3N_4 heterojunctions with different doping ratios were prepared using ice water bath ultrasonography and rapid calcination. The degradation effects on typical antibiotic organic pollutants (TC-HCl) and typical dye organic pollutants with different charge properties [amphoteric dye rhodamine B (RhB), cationic dye methylene blue (MB), and anionic dye methyl orange (MO)] were explored. The performance of photocatalytic nitrogen fixation (NRR and NOR) was investigated using two typical photocatalytic nitrogen fixation conditions. According to the experimental results, the possible mechanisms of the photocatalytic degradation and photocatalytic nitrogen fixation were proposed, which offered a reference for preparing 2D/2D *Z*-scheme heterojunction photocatalysts and photocatalytic degradation and nitrogen fixation.

Experimental

Materials

Sodium tungstate dihydrate ($Na_2WO_4{\cdot}2H_2O$), potassium sodium tartrate tetrahydrate ($C_4H_4KNaO_6{\cdot}4H_2O$), and sodium hydroxide (NaOH) were obtained from Sinopharm Chemical Reagent Co., Ltd. Tetracycline hydrochloride (TC-HCl), rhodamine B (RhB), methylene blue (MB), methyl orange (MO), ammonium oxalate (AO), ammonium chloride (NH_4Cl), potassium nitrate (KNO_3) and potassium mercury iodide (K_2HgI_4) were acquired from Shanghai Maclin Biochemical Co., Ltd. Isopropyl alcohol (IPA), ethanol and methanol were obtained from Beijing Chemical Plant. 65% Nitric acid was derived from Beijing Chemical Plant. Melamine (chemically pure, content $\geq$98%) was purchased from Sigma Aldrich (Shanghai) Trading Co., Ltd. High purity nitrogen (content $\geq$99.999%) and compressed air were acquired from Beijing Millennium Capital Gas Co., Ltd. All solutions in this paper were prepared using ultra-pure water.

Synthesis of 2D/2D *Z*-scheme WO_3/g-C_3N_4 heterojunctions

400 mg of $Na_2WO_4{\cdot}2H_2O$ was added into 300 mL of 4.8 M nitric acid at room temperature for 72 h, centrifugally washed and dried, and ground into a yellow powder as the $WO_3{\cdot}2H_2O$ precursor.[34] 10 g melamine was put into a covered crucible and calcined at 550 °C (heating rate: 5 °C min^{-1}) in a muffle furnace for 4 h. After air cooling, it was ground into a light yellow powder as Bulk g-C_3N_4.[36]

500 mg of Bulk g-C_3N_4 was mixed with $WO_3{\cdot}2H_2O$ of different masses in 20 mL ethanol, ultrasonicated in an ice water bath for 12 h, stirred for 1 hour, and completely dried. The sample underwent rapid calcination at 400 °C for 0.5 h, and was fully ground to obtain the 2D/2D *Z*-scheme WO_3/g-C_3N_4 heterojunctions. WO_3 in the WO_3/g-C_3N_4 composite is the final product of 10 wt.%, 20 wt.%, 30 wt.%, 40 wt.% and 50 wt.%, respectively. They were named as 10% WO_3/g-C_3N_4, 20% WO_3/g-C_3N_4, 30% WO_3/g-C_3N_4, 40% WO_3/g-C_3N_4 and 50% WO_3/g-C_3N_4. Pure WO_3 and pure g-C_3N_4 were prepared for comparison experiments.

Photocatalytic degradation evaluation

The light source was a 300 W Xenon lamp (HX-UV300, Beijing NBET Technology Co., Ltd) equipped with a UVCUT420 ($\lambda \geq$ 420) UV cut-off filter. The optical power meter (CEL-NP2000) monitored the light intensity, and the light intensity was controlled at 100 mW cm^{-2}.

This work used antibiotic organic pollutants TC-HCl and dye organic pollutants MB, RhB and MO as photocatalytic degradation targets. The characteristic peaks of TC-HCl, RhB, MB and MO were 357 nm, 554 nm, 664 nm and 463 nm,[37–39] respectively. The 30 mg photocatalyst was dispersed in 100 mL aqueous solution containing 10 mg L^{-1} organic pollutants, and stirred away from light for 30 min to achieve the adsorption–desorption equilibrium. After the visible-light source was turned on, a 3 mL suspension was taken at certain intervals for centrifugation, and the absorbance of the organic pollutants after degradation was determined by UV-Vis spectrophotometer (YOKE T3202). The degradation efficiency (η) was calculated using the characteristic peak absorbance value. The η was calculated by the eqn (1):[38]

$$\eta = \frac{A_0 - A}{A_0} \times 100\% = \frac{C_0 - C}{C_0} \times 100\% \quad (1)$$

where A_0 and A are the initial absorbance of the characteristic peak of organic pollutants and the absorbance after a certain reaction time, respectively. According to the Lambert–Beer law, C_0 and C are the initial concentration of organic pollutants and the concentration after a certain time, respectively.

Photocatalytic nitrogen fixation evaluation

Experiment 1 and Experiment 2 are two typical conditions of the photocatalytic nitrogen fixation reaction.[34,40,41] The light source was 300 W Xenon lamp (HSX-UV300).

Experiment 1: a 100 mg quantity of photocatalyst was dispersed in 100 mL ultra-pure water, and then ultrasonicated for 15 min. Air flowed into the above suspension at a rate of 100 mL min^{-1}. The suspension was taken at set intervals to test the concentration of NH_4^+ and NO_3^-.[34,41]

Experiment 2: a 100 mg quantity of photocatalyst was dispersed in 100 mL 20% methanol aqueous solution, and then ultrasonicated for 15 min. N_2 flowed into the above suspension at a rate of 100 mL min^{-1}. The suspension was taken at set intervals to test the concentration of NH_4^+ and NO_3^-.[40,41]

The concentration of NH_4^+ was determined by Nessler's reagent colorimetric method. The concentration of NO_3^- was measured by ion chromatography (Shimadzu LC20Adsp, Shodex IC SI-52 4E). The above methods were referred to in our previous paper.[41]

Results and discussion

Photocatalyst characterization

X-ray diffraction spectra (XRD, Rigaku D/MAX-2550V) (Fig. 1(a)) and Fourier-transform infrared (FT-IR, BRUKER VERTEX70) spectra (Fig. 1(b)) were used to characterize the chemical composition and structure of the g-C_3N_4, WO_3 and WO_3/g-C_3N_4 composites. In Fig. 1(a), the characteristic peaks at 13.1° and 27.4° belong to the (100) and (002) crystal faces of pure g-C_3N_4 (JCPDS 87-1526),[33,42] respectively. The (002) peak is attributed to the stacking structure of the conjugated aromatic rings, while the (100) peak is attributed to the interlayer stacking of g-C_3N_4.[43,44] Therefore, after g-C_3N_4 was peeled off by ultrasonic treatment, the intensity of the (100) peak gradually broadened and weakened until it disappeared. The characteristic peaks of pure WO_3 are in accordance with JCPDS 83-0950, which belongs to monoclinic WO_3 (m-WO_3).[45] The XRD results of WO_3/g-C_3N_4 contain the characteristic peaks of g-C_3N_4 and WO_3. With the increase of WO_3 doping amount, the peaks of WO_3 become stronger, while the peaks of g-C_3N_4 become weaker. The XRD results indicate that the WO_3/g-C_3N_4 composites were prepared successfully. These materials maintain the complete crystal structure of the sheet-like g-C_3N_4 and WO_3.

As shown in Fig. 1(b), the FT-IR spectrum of pure WO_3 has a wide peak at 631 cm^{-1} due to the stretching vibration of the O–W–O bond.[46] The peak of pure g-C_3N_4 at 803 cm^{-1} was ascribed to the out-of-plane bending vibration of the 3-*S*-triazine ring. The peaks at 1230 cm^{-1}, 1313 cm^{-1}, 1395 cm^{-1}, 1537 cm^{-1} and 1633 cm^{-1} belong to the skeleton stretching vibration of the C–N heterocyclic ring.[42] All signals of g-C_3N_4 can be seen in the FT-IR spectra of WO_3/g-C_3N_4. With the increase of the WO_3 doping amount, the characteristic peaks of WO_3 gradually become stronger. This is consistent with the XRD results, and indicates the structural integrity of the WO_3/g-C_3N_4 composite.

X-ray photoelectron spectroscopy (XPS, Thermo Fisher Scientific ESCALAB250Xi) was applied to study the surface element composition and valence information of the photocatalysts. Fig. 2(a) shows the XPS full spectrum of g-C_3N_4, WO_3 and 40%WO_3/g-C_3N_4. The XPS survey spectrum of 40%WO_3/g-C_3N_4 shows four elements (C, N, O and W), and no other impurities appear. The C and N are provided by g-C_3N_4, and O and W are provided by WO_3. Fig. 2(b) is the high-resolution W 4f spectrum of WO_3 and 40%WO_3/g-C_3N_4. Compared with the two peaks of pure WO_3 (36.0 eV and 38.1 eV), the two peaks of 40%WO_3/g-C_3N_4 shift to lower binding energy (35.6 eV and 37.7 eV). The reason for this shift may be that the hydrogen

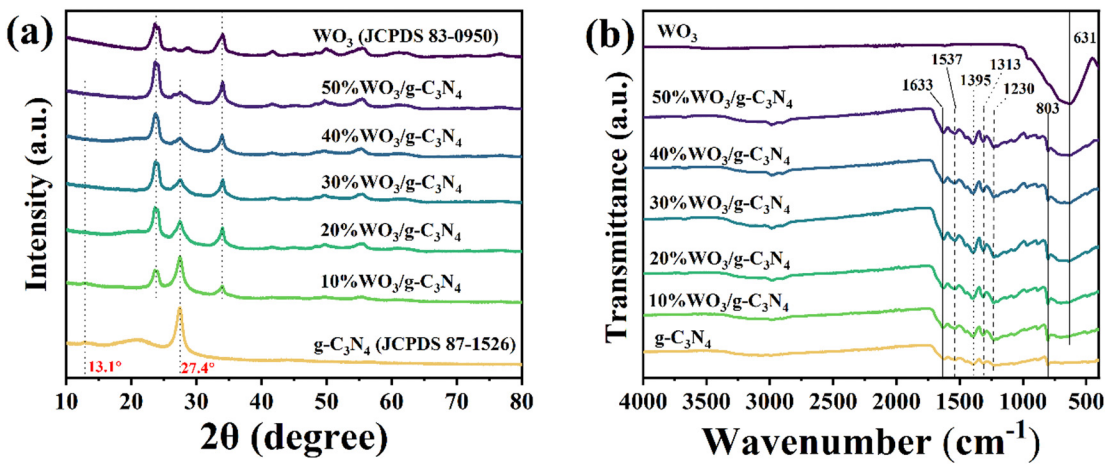

Fig. 1 (a) XRD and (b) FT-IR spectra of the g-C_3N_4, WO_3 and WO_3/g-C_3N_4 composites.

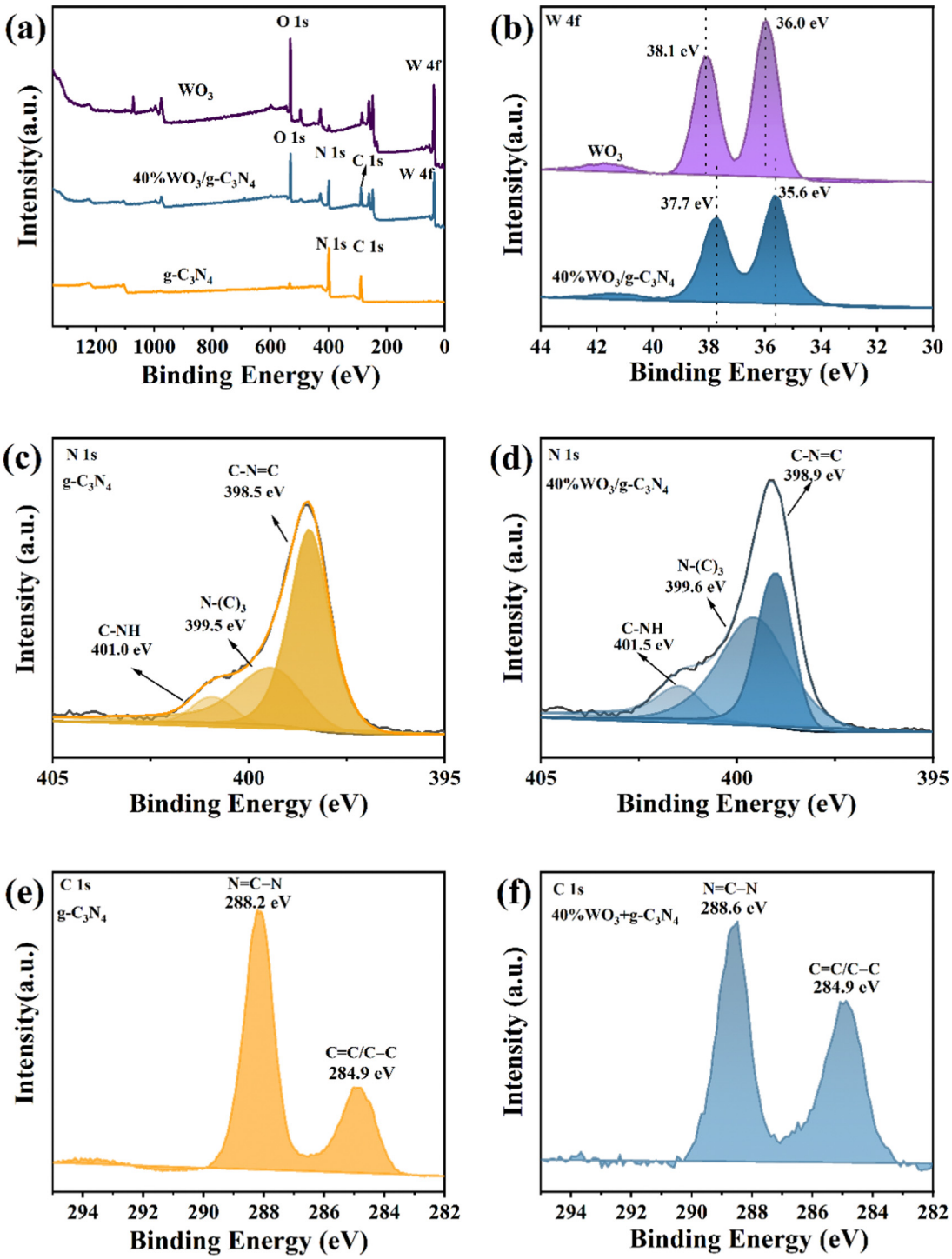

Fig. 2 (a) XPS survey spectra of g-C_3N_4 and 40%WO_3/g-C_3N_4, (b) high-resolution W 4f spectra of WO_3 and 40%WO_3/g-C_3N_4, (c) high-resolution N1s spectra of g-C_3N_4, (d) high-resolution N1s spectra of 40%WO_3/g-C_3N_4, (e) high-resolution C1s spectra of g-C_3N_4 and (f) high-resolution C 1s spectra of 40%WO_3/g-C_3N_4.

bond formed between the terminal –NH_2 and W–O bond during the action of WO_3 and g-C_3N_4 will slightly weaken the W–O bond, thus reducing the binding energy value of W 4f in 40% WO_3/g-C_3N_4.[47,48] Fig. 2(c) and (d) show the high-resolution N 1s spectra of g-C_3N_4 and 40%WO_3/g-C_3N_4, respectively. The positions of the three N1s peaks of pure g-C_3N_4 are 398.5 eV, 399.5 eV and 401.0 eV, which can be attributed to C–N═C, N–$(C)_3$ and C–NH,[49] respectively. The N 1s peaks of 40%WO_3/g-C_3N_4 are shifted towards higher binding energy due to the charge transfer at the interface of WO_3 and g-C_3N_4.[50] This illustrates that a heterostructure is formed between g-C_3N_4 and WO_3. Fig. 2(e) and (f) show the high-resolution C 1s

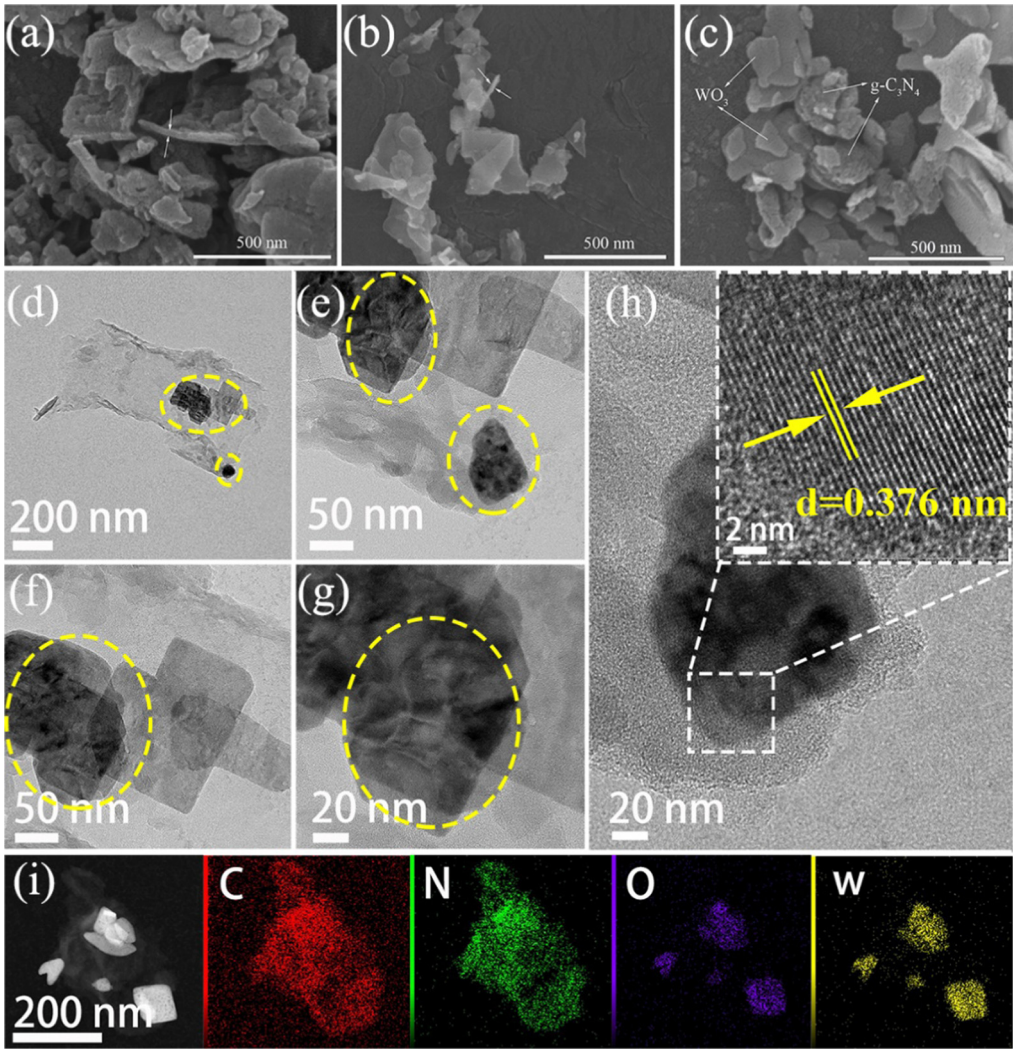

Fig. 3 SEM images of (a) g-C_3N_4, (b) WO_3 and (c) 40%WO_3/g-C_3N_4; (d)–(h) HRTEM images and (i) EDS mapping images of 40%WO_3/g C_3N_4.

spectra of g-C_3N_4 and 40%WO_3/g-C_3N_4, respectively. 40%WO_3/g-C_3N_4 has two major C 1s peaks at 284.9 eV and 288.6 eV, corresponding to sp^2 bonded carbon (N═C–N) and aromatic carbon (C═C/C–C),[19] while the corresponding peaks positions for pure g-C_3N_4 are 284.9 eV and 288.2 eV, respectively. Compared to g-C_3N_4, the position of 40%WO_3/g-C_3N_4 was slightly shifted by 0.4 eV.[50] This is consistent with the results of N1s, verifying the existence of the heterojunction.

The surface morphology of g-C_3N_4, WO_3 and 40%WO_3/g-C_3N_4 can be visually displayed through scanning electron microscope (SEM, Hitachi SU8010) and high-resolution transmission electron microscope (HRTEM, JEOL JEM-F200) with an energy dispersive spectrometer (EDS). As shown by the white arrow in Fig. 3(a), g-C_3N_4 is a stack of nanosheets with a thickness of less than 30 nm. WO_3 is composed of WO_3 nanosheets, which are indicated by the white arrow in Fig. 3(b). Fig. 3(c) shows that 40%WO_3/g-C_3N_4 is a 2D composite structure formed by stacking g-C_3N_4 nanosheets and WO_3 nanosheets together.

Fig. 3(d)–(h) displays the HRTEM images of 40%WO_3/g-C_3N_4. WO_3 is darker than g-C_3N_4, and WO_3 is marked with the yellow circle. The lattice plane of 0.376 nm corresponds to the (002) plane of WO_3 (Fig. 3(h)).[10] The EDS mapping images of 40%WO_3/g C_3N_4 (Fig. 3(i)) demonstrates the existence and the location of the C, N, O and W elements. These results further prove the successful preparation of 2D/2D WO_3/g C_3N_4.

The specific surface area and pore structure of the g-C_3N_4 and WO_3/g-C_3N_4 composites were studied by N_2 adsorption–desorption isotherm (Fig. S1a, ESI†) using Micromeritics ASAP 2460. The pore size distribution diagram (Fig. S1b, ESI†) shows that the pore sizes of these six samples are mainly mesoporous. Among them, the pores of 40%WO_3/g-C_3N_4 are mainly distributed in the 1.5–16 nm range, and there are few mesopores smaller than 2 nm.[51] Table S1 (ESI†) summarizes the data for the specific surface area and pore volume. The specific surface areas of the WO_3/g-C_3N_4 composites are all smaller than that of pure g-C_3N_4, and 20%WO_3/g-C_3N_4 (11.88 m^2 g^{-1}) has the smallest specific surface area. The specific surface area sizes of 40% WO_3/g-C_3N_4 (14.87 m^2 g^{-1}) and 50% WO_3/g-C_3N_4 (14.90 m^2 g^{-1}) are similar. For the pore volume, the pure g-C_3N_4 (0.49 cm^3 g^{-1}) is still the largest, and 20% WO_3/g-C_3N_4

($0.04\ cm^3\ g^{-1}$) is the smallest. The specific surface area and pore volume can affect the number of active sites, and thus affect the adsorption and reaction effect in the catalytic process. However, the specific surface area and pore volume are not necessarily better with larger sizes. It is necessary to synthesize other properties to obtain the final catalytic performance. Table S1 (ESI†) also shows the zeta potential of the g-C_3N_4 and WO_3/g-C_3N_4 composites in water.

Fig. 4(a) shows the results from investigating the optical properties of the g-C_3N_4, WO_3 and WO_3/g-C_3N_4 composites by ultraviolet and visible diffuse reflectance spectra (UV-Vis DRS, SHIMADZU UV-3600 Plus). Fig. 4(a) was converted into Fig. 4(b) using the Kubelka–Munk function, and the band gap (E_g) of the g-C_3N_4, WO_3 and WO_3/g-C_3N_4 composites was estimated.[41] The E_g values of pure g-C_3N_4 and pure WO_3 are 2.48 eV and 2.41 eV, respectively. The similar E_g of these two pure substances leads to the similar E_g of the WO_3/g-C_3N_4 composites, which is why the g-C_3N_4, WO_3 and WO_3/g-C_3N_4 composites are all yellow. The E_g of 40%WO_3/g-C_3N_4 and 50%WO_3/g-C_3N_4 is 2.43 eV, which is the smallest E_g among the five WO_3/g-C_3N_4 composites and is more conducive to the absorption of visible light.

To further study the photogenerated carrier recombination probability of the g-C_3N_4 and WO_3/g-C_3N_4 composites, the photoluminescence (PL, HORIBA FluoroMax-4) spectra of the samples were tested. The weak PL peak intensity indicates the low recombination probability of the photogenerated carriers and high separation efficiency.[43,52] As shown in Fig. 4(c), the PL peak intensity was ranked as g-C_3N_4 > 30%WO_3/g-C_3N_4 > 10%WO_3/g-C_3N_4 > 20%WO_3/g-C_3N_4 > 50%WO_3/g-C_3N_4 > 40% WO_3/g-C_3N_4. The 40%WO_3/g-C_3N_4 photogenerated carrier recombination rate is the lowest in the above samples. Thus, the photogenerated e^-–h^+ separation efficiency of 40%WO_3/g-C_3N_4 is the highest, which is conducive to improving its photocatalytic performance.

Electrochemical impedance spectroscopy (EIS, CHI660E Electrochemical Workstation) was used to further investigate the charge transfer capability of the g-C_3N_4, WO_3 and 40% WO_3/g-C_3N_4 (Fig. 4(d)).[41] A smaller arc radius on the EIS Nyquist diagram corresponds to a smaller charge transfer resistance on the working electrode surface.[41] In Fig. 4(d), the arc radius of 40% WO_3/g-C_3N_4 is smaller than that of g-C_3N_4 and WO_3, illustrating that 40% WO_3/g-C_3N_4 has better photogenerated electron–hole separation and transfer ability.

Photocatalytic degradation performance

Firstly, the photocatalyst and TC-HCl were mixed away from light for 30 min (t is −30 to 0 min in the corresponding Fig. 5(a)) to reach the adsorption–desorption equilibrium. The degradation efficiencies of the g-C_3N_4, WO_3 and WO_3/g-C_3N_4 composites as a photocatalyst for the antibiotic organic pollutant TC-HCl are shown in Fig. 5(a). The adsorption efficiency of the g-C_3N_4, WO_3 and WO_3/g-C_3N_4 composites for TC-HCl is about 7%. The adsorption rate of pure WO_3 to TC-HCl is slower than that of the g-C_3N_4 and WO_3/g-C_3N_4 composites, while the adsorption of bulk g-C_3N_4 to TC-HCl was almost zero. When t is 0 min, the visible light

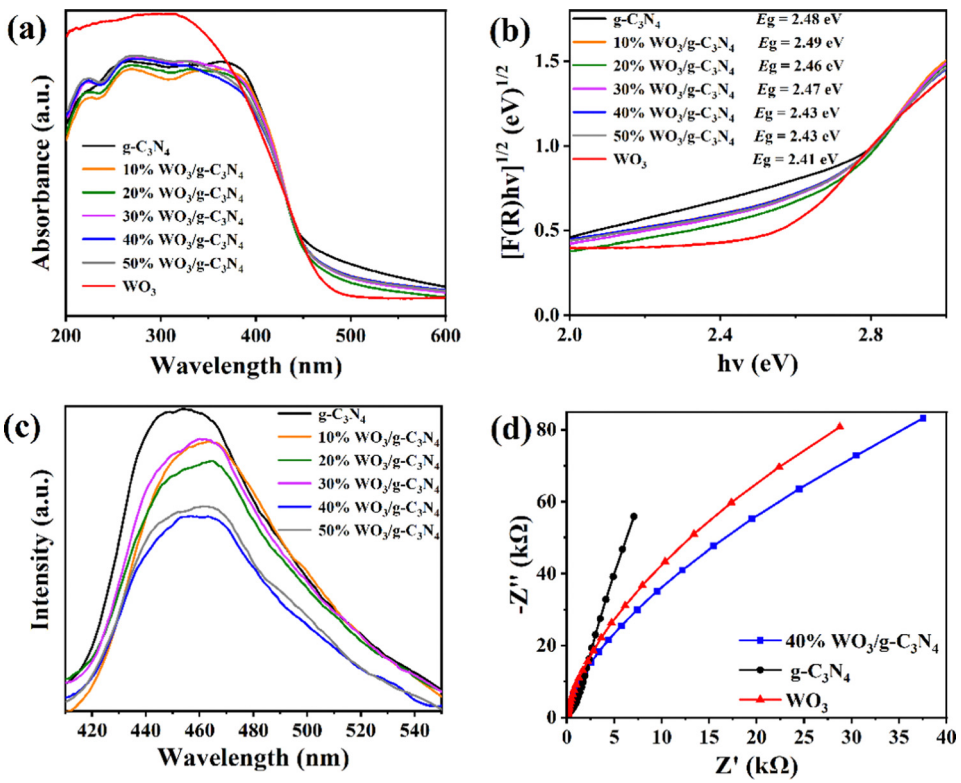

Fig. 4 (a) UV-vis DRS spectra, (b) E_g and (c) PL spectra of the g-C_3N_4, WO_3 and WO_3/g-C_3N_4 composites; (d) EIS of 40%WO_3/g-C_3N_4, g-C_3N_4 and WO_3.

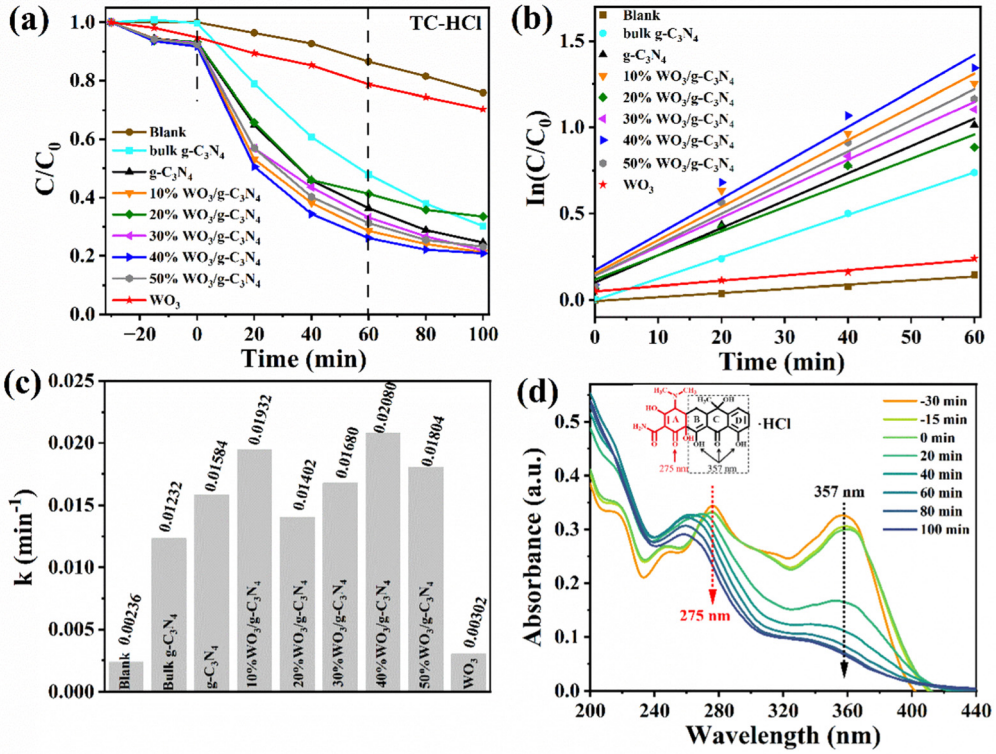

Fig. 5 (a) The photocatalytic degradation efficiency of TC-HCl by g-C_3N_4, WO_3 and WO_3/g-C_3N_4 composites under visible light, (b) corresponding first-order kinetic fitting curves and (c) corresponding UV-vis absorption spectra during the degradation of TC-HCl by 40%WO_3/g-C_3N_4.

source was turned on to start the photocatalytic reaction. "Blank" is the blank control without any photocatalyst. The self-degradation rate of TC-HCl is 24.1% after 100 min visible-light irradiation. The removal efficiency of TC-HCl by bulk g-C_3N_4, g-C_3N_4, WO_3, 10%WO_3/g-C_3N_4, 20%WO_3/g-C_3N_4, 30%WO_3/g-C_3N_4, 40%WO_3/g-C_3N_4 and 50%WO_3/g-C_3N_4 are 69.8%, 75.4%, 29.7%, 78.8%, 66.6%, 78.1%, 79.1% and 76.9%, respectively. It shows that 40%WO_3/g-C_3N_4 has the best degradation effect on TC-HCl. The degradation rate of the WO_3/g-C_3N_4 composite became slow after the irradiation time t was 60 min, indicating that the maximum degradation efficiency was reached at 60 min. Therefore, t was 0–60 min for the first-order kinetic fitting (Fig. 5(b)). Fig. 5(a) shows the degradation process, and Fig. 5(b) shows the first-order kinetics fitting curve, which was calculated by eqn (2):

$$-\ln\left(\frac{C}{C_0}\right) = kt \quad (2)$$

where C_0 and C are the concentrations of the organic pollutants (mg L^{-1}, ppm) in water at the initial concentration and time t, respectively. The term k is the apparent rate constant (min^{-1}).

Fig. 5(c) is a histogram comparison of the apparent rate constant k. The k values of bulk g-C_3N_4, g-C_3N_4, WO_3, 10%WO_3/g-C_3N_4, 20%WO_3/g-C_3N_4, 30%WO_3/g-C_3N_4, 40%WO_3/g-C_3N_4 and 50%WO_3/g-C_3N_4 were 0.00236 min^{-1}, 0.01232 min^{-1}, 0.01584 min^{-1}, 0.00302 min^{-1}, 0.01932 min^{-1}, 0.01402 min^{-1}, 0.01680 min^{-1}, 0.02080 min^{-1} and 0.01804 min^{-1}, respectively. Therefore, the introduction of the g-C_3N_4 nanosheets is greatly enhanced the catalytic effect of WO_3. Among them, 40%WO_3/g-C_3N_4 had the best degradation efficiency, which was 1.69 times, 1.31 times and 6.89 times of bulk g-C_3N_4, g-C_3N_4 and WO_3, respectively.

Fig. 5(d) shows the UV-visible absorption spectrum during the adsorption and degradation of TC-HCl by 40%WO_3/g-C_3N_4. TC-HCl has two characteristic peaks at 275 nm and 357 nm, as shown in Fig. 5(d). It has been reported that the peak at 275 nm is associated with the aromatic ring A structure, including the enolic hydroxyl, amide and ketone groups. The peak at 357 nm is from aromatic rings B, C, and D, comprising the extended chromophores.[53] 40%WO_3/g-C_3N_4 can simultaneously destroy the rings B, C, D, and A, but the destructive effect on A is relatively weak under visible light. The slight shift in the location of the characteristic peak may be caused by the slight change in pH during the removal process.

Fig. 6(a) shows the removal process of 40%WO_3/g-C_3N_4 as a photocatalyst for three typical dyes with different charge properties, cationic dye MB, amphoteric dye RhB, and anionic dye MO. After 30 min dark adsorption process, 11.4% MB, 24.6% RhB and 1.8% MO can be removed. According to Table S1 (ESI†), 40%WO_3/g-C_3N_4 was negatively charged in water, so the adsorption effect of the anionic dye MO was poor. When the light source was turned on, RhB was almost completely degraded after 20 min. After 100 min, the total removal rate of MB reached 91.4%, while that of MO was only 49.6%. Therefore, it proves that 40%WO_3/g-C_3N_4 has a good removal effect on MB and RhB.

Fig. 6(b) shows the recycling experiments of 40%WO_3/g-C_3N_4, where it can be seen that 40%WO_3/g-C_3N_4 almost

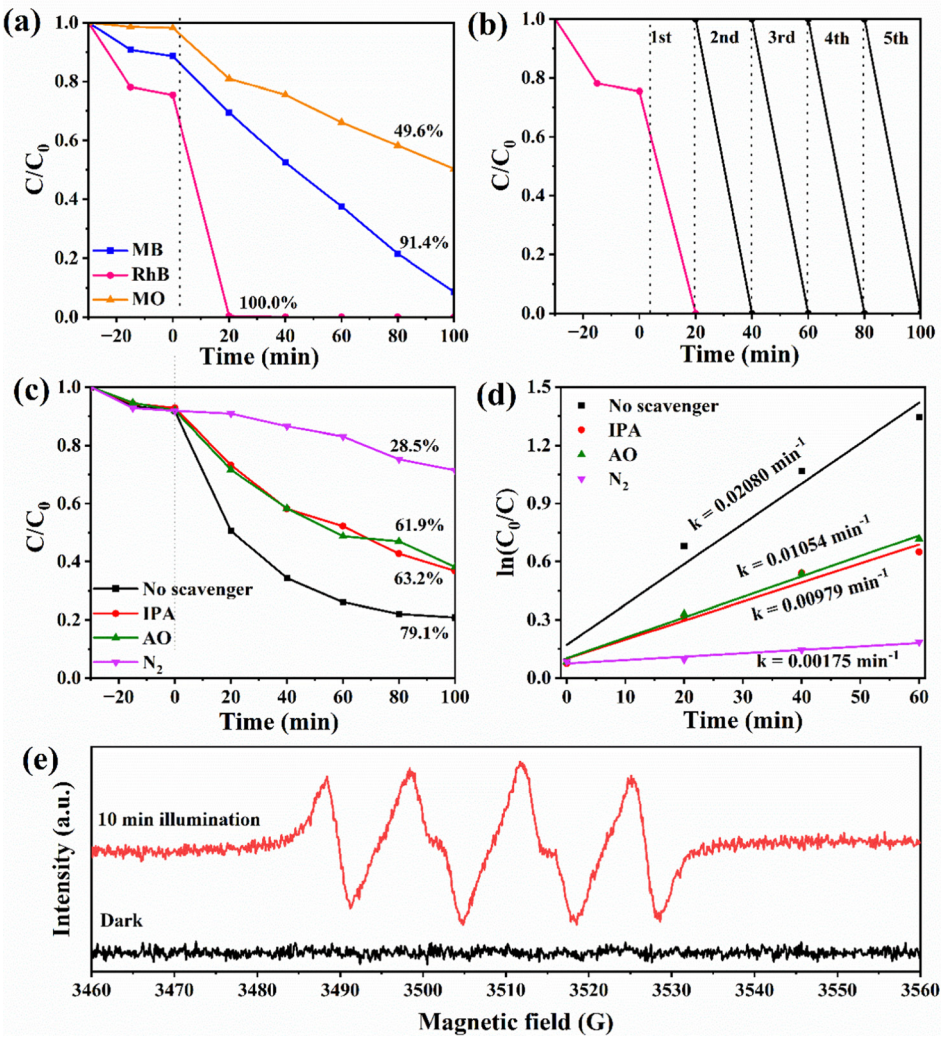

Fig. 6 (a) The removal process of MB, RhB and MO by 40%WO_3/g-C_3N_4. (b) Photodegradation cycle test of 40%WO_3/g-C_3N_4; (c) free radical capture experiments of the 0.3 g L^{-1} 40%WO_3/g-C_3N_4 photocatalytic degradation of 10 mg L^{-1} TC-HCl, and (d) their first-order kinetic fitting curves; and (e) EPR spectra of the DMPO-$^{\bullet}O_2^-$ adducts over 40%WO_3/g-C_3N_4 under dark condition and with 10 min illumination in methanol.

maintained its original degradation efficiency of RhB after 5 cycles. Therefore, 40%WO_3/g-C_3N_4 possessed good photocatalytic stability for the potential application.

Photocatalytic degradation mechanism

It has been reported that the superoxide radical ($^{\bullet}O_2^-$), hole (h^+), and hydroxyl radical ($^{\bullet}OH$) are the main active species in photocatalytic oxidation reactions.[54] To study the photocatalytic degradation mechanism of the 40%WO_3/g-C_3N_4 photocatalyst, three trapping agents were applied to explore the active species in the photocatalytic reaction process. In this work, 1 mM ammonium oxalate (AO) was used to capture h^+, and 1 mM isopropyl alcohol (IPA) was used to capture $^{\bullet}OH$. N_2 is used to remove O_2 in the reaction system. It blocked the generation of $^{\bullet}O_2^-$ from the root. Therefore, N_2 can be used as the trapping agent of $^{\bullet}O_2^-$.[55] By adding different trapping agents in the reaction solution, the corresponding reactive species were removed. According to the change of photocatalytic efficiency, the role of different active substances in the photocatalytic process can be determined. The device and process of the above capture experiment are the same as that of the photocatalytic performance test.

Fig. 6(c) shows the degradation process of 10 mg L^{-1} TC-HCl by 0.3 g L^{-1} 40%WO_3/g-C_3N_4 when IPA, AO and N_2 were added to the reaction system. The removal rate decreased from 79.1% to 63.2%, 61.9% and 28.5%, respectively. It indicated that N_2 has the greatest impact on the removal rate. Therefore, $^{\bullet}O_2^-$ was the main active species, while h^+ and $^{\bullet}OH$ had similar effects as the minor active species. Fig. 6(d) shows the kinetic fitting curves for the photocatalytic process that is shown in Fig. 6(c). The first 60 min of the reaction process conforms to the first-order kinetic model. The apparent rate constants k decreased from 0.02080 min^{-1} to 0.00979 min^{-1}, 0.01054 min^{-1} and 0.00175 min^{-1}, respectively (Fig. 6(d)). This verifies that the role of the active species in this process is ranked as $^{\bullet}O_2^- > h^+ \approx {}^{\bullet}OH$.

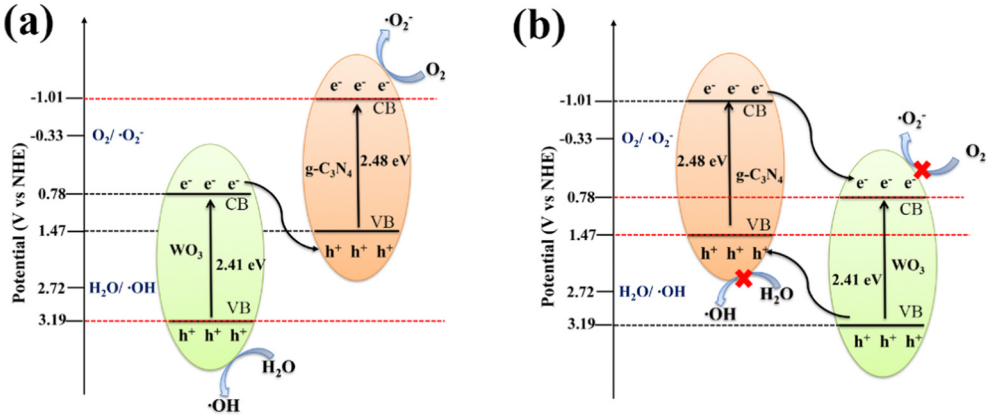

Fig. 7 The proposed mechanisms for the degradation of organic pollutants by 40%WO_3/g-C_3N_4 (a) *Z*-scheme heterojunction and (b) type-II heterojunction.

The valence band potential (E_{VB}) and conduction band potential (E_{CB}) of the semiconductor zero charge point (pH_{zpc}) can be estimated by eqn (3) and (4):[56–60]

$$E_{VB} = X - E_e + 0.5E_g \quad (3)$$

$$E_{CB} = E_{VB} - E_g \quad (4)$$

where X is the geometric mean of the absolute electronegativity of the constituent atoms of the semiconductor, E_e is the energy of the free electron at the hydrogen scale, and E_g is the band gap. The X values of g-C_3N_4 and WO_3 were 4.73 eV and 6.49 eV, respectively.[54] According to eqn (3) and (4), it can be estimated that the E_{CB} values of g-C_3N_4 and WO_3 are −1.01 eV and 0.78 eV, respectively. The E_{VB} values of g-C_3N_4 and WO_3 are 1.47 eV and 3.19 eV, respectively.

Whether the $^{\bullet}O_2^-$ species are generated over 40% WO_3/g-C_3N_4 under light irradiation offers an important clue to determining the transfer route of the charge carriers. $\cdot O_2^-$ was detected using electron paramagnetic resonance (EPR, Bruker EMXplus-6/1). In Fig. 6(e), the apparent $^{\bullet}O_2^-$ characteristic peaks can be observed in the EPR spectrum of 5,5-dimethyl-1-pyrroline N-oxide (DMPO)- $^{\bullet}O_2^-$ adduct over 40% WO_3/g-C_3N_4 after 10 min light illumination, demonstrating the generation of $^{\bullet}O_2^-$.[61,62]

According to the results of the above capture experiments and EPR, two possible reaction mechanisms are proposed in Fig. 7. The electron (e^-) on the CB of WO_3 and h^+ on VB of g-C_3N_4 in the *Z*-scheme 40%WO_3/g-C_3N_4 heterojunction (Fig. 7(a)) are recombined. The CB of g-C_3N_4 is more negative than $O_2/^{\bullet}O_2^-$ (−0.33V *vs.* NHE), and the VB of WO_3 is more positive than $H_2O/^{\bullet}OH$ (2.72V vs NHE), which allows $^{\bullet}O_2^-$ and $^{\bullet}OH$ to be produced. If g-C_3N_4 and WO_3 form a conventional type-II heterojunction (Fig. 7(b)), the CB of g-C_3N_4 will transfer e^- to the CB of WO_3, while the VB of WO_3 will transfer h^+ to the VB of g-C_3N_4. However, in this case, the CB of WO_3 will be more positive than $O_2/^{\bullet}O_2^-$, so that the electrons on CB cannot reduce O_2 to generate $^{\bullet}O_2^-$.[47] At the same time, the VB of g-C_3N_4 will be more negative than $H_2O/^{\bullet}OH$, so that the h^+ in VB cannot oxidize H_2O to generate $^{\bullet}OH$.[47] In conclusion, 40%WO_3/g-C_3N_4 is the *Z*-scheme heterojunction. This structure can improve the separation of the photogenerated e^- and h^+, and enhance the redox ability of the photogenerated e^- and h^+, as well as the catalytic performance of the photocatalyst.[9–16]

In addition, the comparison of almost all published 2D/2D *Z*-scheme WO_3/g-C_3N_4 heterojunction systems is shown in Table 1, which indicates that the facile synthetic 2D/2D *Z*-scheme WO_3/g-C_3N_4 heterojunctions in this work exhibit considerable photocatalytic performance in the environmental application and energy application without any cocatalyst.[9–16]

Table 1 Comparison of the 2D/2D *Z*-schemes of the WO_3/g-C_3N_4 heterojunction photocatalyst systems

Photocatalyst	Synthesis	Environmental application	Energy application	Ref.
$WO_3 \cdot H_2O$/g-C_3N_4	Ultrasonic-assisted self-assembly	95% RhB degradation in 80 min	—	9
WO_3/Ag/CN	Solvent evaporation and *in situ* calcination	96.2% RhB degradation in 40 min; ~90% TC degradation in 140 min	—	10
WO_3/CNT/g-C_3N_4	Wet impregnation	92.3% MO degradation in 60 min	H_2 production	11
Pt-*g*-C_3N_4/H-WO_3	Post-annealing	—	H_2 production	12
WO_3/RGO/H-*g*-C_3N_4	Microwave-assisted hydrothermal method	~90% TC-HCl degradation in 60 min	—	13
WO_3/g-C_3N_4	*In situ* construction	~100% RhB degradation in 40 min	—	14
Pt–WO_3/g-C_3N_4	Reverse microemulsion	—	H_2 production	15
g-C_3N_4/Si-O/WO_3	Wet chemical method	—	Aerobic alcohol oxidation	16
WO_3/g-C_3N_4	**Rapid calcination**	**79.1% TC-HCl, 91.4% MB and 49.6% MO degradation in 100 min, respectively; ~100% RhB degradation in 20 min**	**Nitrogen fixation (NNR and NOR)**	**This work**

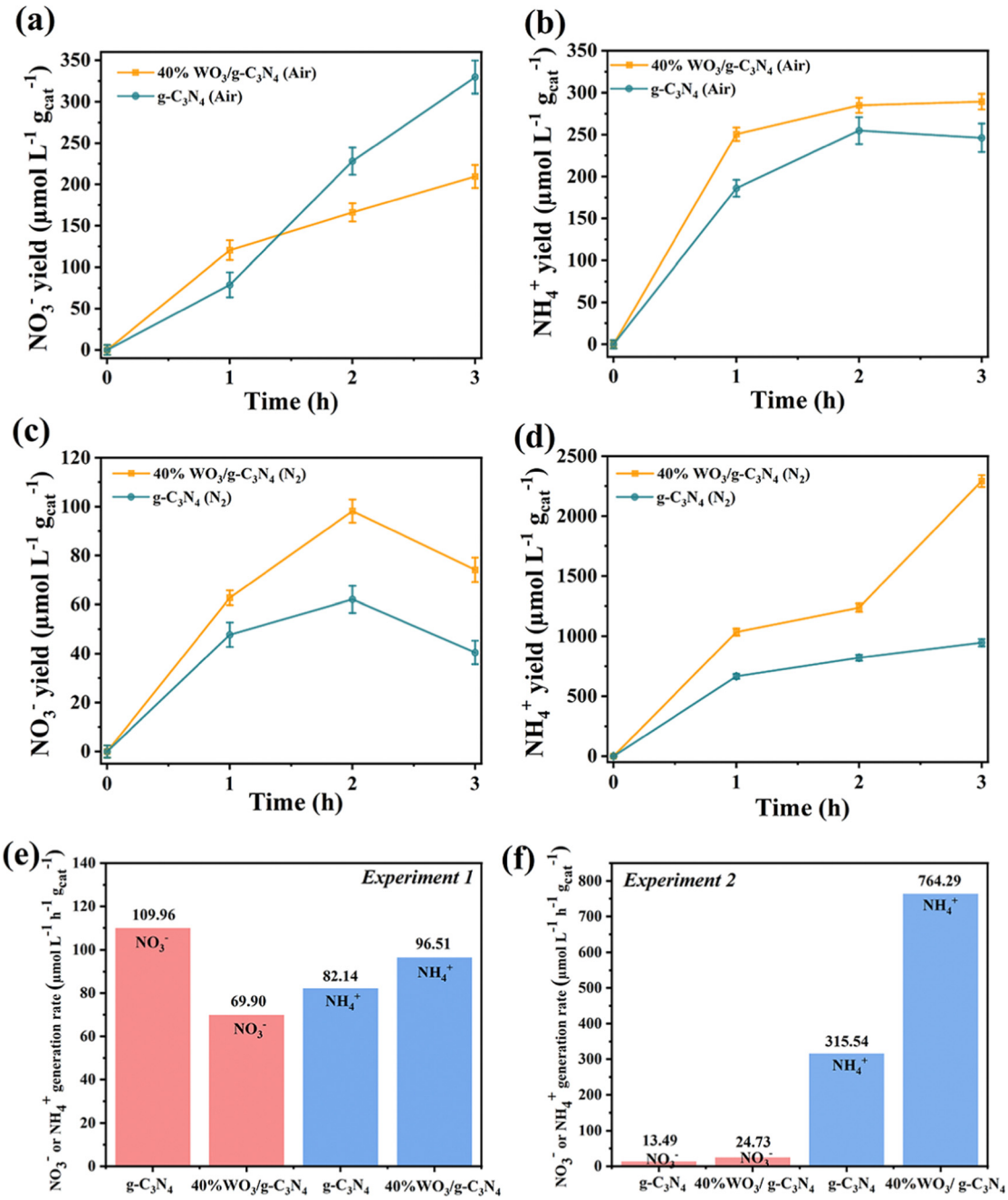

Fig. 8 Photocatalytic nitrogen fixation performance of 40%WO_3/g-C_3N_4 and g-C_3N_4: (a) the yield of NO_3^- in experiment 1, (b) the yield of NH_4^+ in Experiment 1, (c) the yield of NO_3^- in Experiment 2, and (d) the yield of NH_4^+ in Experiment 2. Error bars represent the standard deviation of three independent experiments. (e) The 3 h average NO_3^- or NH_4^+ generation rate in Experiment 1 of g-C_3N_4 and 40%WO_3/g-C_3N_4, and (f) the 3 h average NO_3^- or NH_4^+ generation rate in Experiment 2 of g-C_3N_4 and 40%WO_3/g-C_3N_4.

Photocatalytic nitrogen fixation performance

Fig. 8(a), (b) and (e) show the generation of NO_3^- and NH_4^+ in Experiment 1. As shown in Fig. 8(a), when the air was introduced into the aqueous suspension of 40%WO_3/g-C_3N_4 under Xenon lamp irradiation, the NO_3^- concentration increased with the increase of the reaction time. After 1 h, the NO_3^- yield decreased, and the amount of the NO_3^- yield was lower than that of pure g-C_3N_4. As shown in Fig. 8(b), the yield of NH_4^+ first increased for 1 h and then gradually stabilized. At the same time, the yield was always higher than that of pure g-C_3N_4. Fig. 8(e) shows that the 3 h average NO_3^- yield of 40%WO_3/g-C_3N_4 was 69.90 μmol L^{-1} h^{-1} g_{cat}^{-1}, and the 3 h average NH_4^+ yield was 96.51 μmol L^{-1} h^{-1} g_{cat}^{-1}. Unlike pure g-C_3N_4, the yield of the nitrogen fixed product NO_3^- in the N_2 disproportionation reaction of 40%WO_3/g-C_3N_4 was lower than that of NH_4^+. The total nitrogen fixation efficiency of 40%WO_3/g-C_3N_4 was 166.41 μmol L^{-1} h^{-1} g_{cat}^{-1}, which was lower than that of pure g-C_3N_4 (192.10 μmol L^{-1} h^{-1} g_{cat}^{-1}). Therefore, the

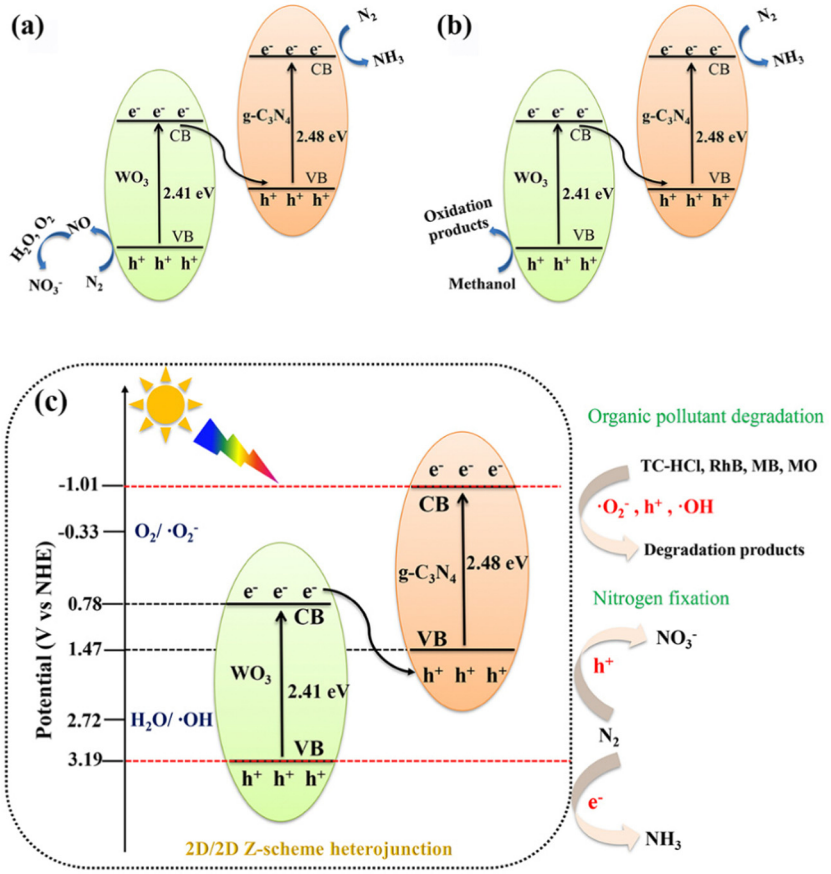

Fig. 9 The proposed photocatalytic nitrogen fixation mechanism of 40%WO_3/g-C_3N_4: (a) Experiment 1 and (b) Experiment 2; and (c) the proposed photocatalytic mechanism of the 2D/2D *Z*-scheme WO_3/g-C_3N_4 heterojunctions in this work.

nitrogen disproportionation reaction efficiency of 40%WO_3/g-C_3N_4 in Experiment 1 was lower than that of pure g-C_3N_4 and the NRR accounted for a larger proportion in the disproportionation reaction.

The generation of NO_3^- and NH_4^+ in Experiment 2 is shown in Fig. 8(c), (d) and (f). When N_2 was introduced into a 20% methanol (as hole scavenger) aqueous suspension containing 40%WO_3/g-C_3N_4 under Xenon lamp irradiation, the NO_3^- yield first increased and then decreased (Fig. 8(c)). In the 2 hours, a small amount of NO_3^- was produced due to the removal of h^+. After 2 hours, the e^- reduce NO_3^- and the NO_3^- yield decreased. For Fig. 8(d), the NH_4^+ yield continued to increase. In addition, the NH_4^+ yield of 40%WO_3/g-C_3N_4 was 2.37 times higher than that of pure g-C_3N_4. Fig. 8(f) shows that the 3 h average NO_3^- yield of 40%WO_3/g-C_3N_4 was 24.73 μmol L^{-1} h^{-1} g_{cat}^{-1}, and the 3 h average NH_4^+ yield was 764.29 μmol L^{-1} h^{-1} g_{cat}^{-1}. NH_4^+ was the main nitrogen fixation product. The total nitrogen fixation efficiency of 40%WO_3/g-C_3N_4 (789.02 μmol L^{-1} h^{-1} g_{cat}^{-1}) was 2.40 times higher than that of the g-C_3N_4 nanosheets (329.03 μmol L^{-1} h^{-1} g_{cat}^{-1}). Experiment 2 showed that 40% WO_3/g-C_3N_4 enhanced the NRR.

Photocatalytic nitrogen fixation mechanism

A photocatalytic nitrogen fixation mechanism based on the 40%WO_3/g-C_3N_4 *Z*-scheme heterojunction was proposed, as shown in Fig. 9(a) and (b). Under light irradiation, 40%WO_3/g-C_3N_4 generated photogenerated electron–hole (e^-–h^+) pairs on VB. Then, e^- was transferred from VB to CB while leaving h^+ on VB. In Experiment 1 (Fig. 9(a)), the photogenerated e^- on VB can be transferred to the surface *via* nitrogen vacancies. Then, e^- can reduce N_2 (in the incoming air) to NH_3. At the same time, the remaining photogenerated h^+ in VB can oxidize N_2 (in the incoming air) to NO. Then, NO further reacts with O_2 and H_2O to generate NO_3^-.[31,34]

In Experiment 1, N_2 underwent a disproportionation reaction to generate NH_4^+ and NO_3^-. It has been reported that the disproportionation reactions are energetically more favorable than the individual oxidation or reduction reactions.[31] According to the law of charge conservation, the ratio of NO_3^- to NH_4^+ generated in the N_2 dismutation reaction should be 3 : 5.[31] Nevertheless, the actual ratio of NO_3^- to NH_4^+ is closer to 5 : 7. The slightly lower proportion of NH_4^+ is due to the competition from the hydrogen evolution reaction (HER). In Experiment 1, 40%WO_3/g-C_3N_4 with the *Z*-scheme heterojunction was not more effective than pure g-C_3N_4. This is because g-C_3N_4 is beneficial to the adsorption and activation of N_2, and the active ingredient of 40%WO_3/g-C_3N_4 is mainly on the VB of WO_3. The adsorbed and activated N_2 on g-C_3N_4 is far from h^+, which results in reduced NOR efficiency.

However, in Experiment 2 (Fig. 9(b)), the photogenerated h^+ was consumed by the hole sacrifice agent, which highlighted

the advantage of the 40%WO_3/g-C_3N_4 *Z*-scheme heterojunction. A large amount of photogenerated e^- could reduce N_2 to NH_3 and improve the NRR reaction efficiency. Therefore, 40%WO_3/g-C_3N_4 is suitable for photocatalytic nitrogen fixation, reducing N_2 to ammonia. The reaction conditions of nitrogen fixation have a great influence on the reaction products of nitrogen fixation.

Conclusions

A series of 2D/2D *Z*-scheme WO_3/g-C_3N_4 heterojunctions were prepared by facile rapid calcination, and the degradation effect of different WO_3 ratios on the typical antibiotic organic contaminant TC-HCl was explored. The photocatalytic degradation effect of 40%WO_3/g-C_3N_4 is 1.69, 1.31 and 6.89 times higher than that of bulk g-C_3N_4, g-C_3N_4 and WO_3 nanosheets, respectively. The removal efficiency of RhB, MB and MO were 100%, 91.4% and 49.6%, respectively. The main reactive species of 40%WO_3/g-C_3N_4 in the degradation process was $^{\bullet}O_2^-$. The 2D/2D *Z*-scheme WO_3/g-C_3N_4 can realize photocatalytic nitrogen fixation. With the presence of a hole sacrifice agent and N_2 as the nitrogen source, the photocatalytic nitrogen fixation reaction of 40%WO_3/g-C_3N_4 was dominated by NRR, and the almost all product was NH_4^+ (764.29 μmol L^{-1} h^{-1} g_{cat}^{-1}). The total nitrogen fixation efficiency was 2.40 times higher than that of pure g-C_3N_4. The results prove that the 2D/2D *Z*-scheme heterojunction enhanced the photogenerated electron–hole separation and transfer ability, which is very effective in both photocatalytic degradation and photocatalytic nitrogen fixation application scenarios (Fig. 9(c)). This work provides a reference for understanding the 2D/2D *Z*-scheme heterojunctions, photocatalytic NRR and NOR reactions, and the photocatalytic degradation process of antibiotics and organic pollutants with different charge properties.

Author contributions

Yasi Li contributed to the experimental design, investigation, validation, and writing of the original draft. Junkai Wang performed the conceptualization, methodology, investigation, visualization, and funding acquisition.

Conflicts of interest

There are no conflicts to declare.

Acknowledgements

This work was funded by the Special Program for Science Research Foundation of the Higher Education Institutions of Guangdong Providence (grant no. 2020ZDZX2052), and the Shantou University Scientific Research Foundation for Talents (grant no. NTF22004).

References

1 J. Bai, R. Shen, Z. Jiang, P. Zhang, Y. Li and X. Li, *Chin. J. Catal.*, 2022, **43**, 359–369.
2 Y. Hu, X. Li, W. Wang, F. Deng, L. Han, X. Gao, Z. Feng, Z. Chen, J. Huang, F. Zeng and F. Dong, *Chin. J. Struct. Chem.*, 2022, **41**, 2206069.
3 G. M. Li, B. Wang and R. Wang, *Chin. J. Struct. Chem.*, 2020, **39**, 1675–1688.
4 Z. Jin, Y. Li and X. Hao, *Acta Phys.-Chim. Sin.*, 2021, **37**, 1912033.
5 X. Li, B. Wang, W. Yin, J. Di, J. Xia, W. Zhu and H. Li, *Acta Phys.-Chim. Sin.*, 2020, **36**, 17401.
6 L. Huang, H. Xu, Y. Li, H. Li, X. Cheng, J. Xia, Y. Xu and G. Cai, *Dalton Trans.*, 2013, **42**, 8606–8616.
7 Y. Y. Zhou, J. X. Zhang and D. F. Wu, *ChemistrySelect*, 2023, **8**, e202301237.
8 K. He, J. Xie, X. Luo, J. Wen, S. Ma, X. Li, Y. Fang and X. Zhang, *Chin. J. Catal.*, 2017, **38**, 240–252.
9 L. Li, D. Jiang, X. Wu, X. Sun, X. Qu, L. Shi and F. Du, *J. Mater. Sci.*, 2020, **55**, 4238–4250.
10 J. Chen, X. Xiao, Y. Wang and Z. Ye, *Appl. Surf. Sci.*, 2019, **467–468**, 1000–1010.
11 U. Bharagav, N. R. Reddy, V. N. K. Rao, P. Ravi, M. Sathish, D. Rangappa, K. Prathap, C. S. Chakra, M. V. Shankar, L. Appels, T. M. Aminabhavi, R. R. Kakarla and M. M. Kumari, *Chemosphere*, 2023, **311**, 137030.
12 D. Liu, S. Zhang, J. Wang, T. Peng and R. Li, *ACS Appl. Mater. Interfaces*, 2019, **11**, 27913–27923.
13 Y. Bao, H. Guo, L. Jiang, Z. Liu, J. Qu, C. Zhang, X. Jia and K. Chen, *Appl. Surf. Sci.*, 2019, **496**, 143639.
14 H. Zhang, Z. Cai, W. Xu, M. Huang and X. Liu, *New J. Chem.*, 2019, **43**, 17416.
15 S. Tang, Y. Ma, H. Wang, Y. Liang, X. Xu, D. Zhang, B. Cao, Q. Wang and W. Li, *ChemSusChem*, 2023, **16**, e202202184.
16 L. Sun, B. Li, X. Chu, N. Sun, Y. Qu, X. Zhang, I. Khan, L. Bai and L. Jing, *ACS Sustainable Chem. Eng.*, 2019, **7**, 9916–9927.
17 Z. B. Wu, X. Z. Yuan, J. Zhang, H. Wang, L. B. Jiang and G. M. Zeng, *ChemCatChem*, 2017, **9**, 41–64.
18 E. Forgacs, T. Cserhati and G. Oros, *Environ. Int.*, 2004, **30**, 953–971.
19 X. R. Yang, Z. Chen, W. Zhao, C. X. Liu, X. X. Qian, M. Zhang, G. Y. Wei, E. Khan, Y. H. Ng and Y. S. Ok, *Chem. Eng. J.*, 2021, **405**, 126806.
20 H. Yang, Z. C. Zhao, Y. P. Yang, Z. Zhang, W. Chen, R. Q. Yan, Y. X. Jin and J. Zhang, *Sep. Purif. Technol.*, 2022, **300**, 121846.
21 Y. X. Li, M. Fu, R. Q. Wang, S. W. Wu and X. M. Tan, *Chem. Eng. J.*, 2022, **444**, 136567.
22 J. Guo, T. T. Liu, H. Peng and X. G. Zheng, *Int. J. Mol. Sci.*, 2022, **23**, 9343.
23 F. D. Wu, J. C. Chen and J. P. Hu, *J. Environ. Chem. Eng.*, 2022, **10**, 107117.
24 S. Krobthong, T. Rungsawang and S. Wongrerkdee, *Toxics*, 2023, **11**, 266.
25 G. H. Dong, W. K. Ho and C. Y. Wang, *J. Mater. Chem. A*, 2015, **3**, 23435–23441.

26 J. H. Yang, H. Y. Bai, Y. Z. Guo, H. Zhang, R. B. Jiang, B. C. Yang, J. F. Wang and J. C. Yu, *Angew. Chem., Int. Ed.*, 2021, **60**, 927–936.
27 P. F. Xia, X. C. Pan, S. L. Jiang, J. G. Yu, B. W. He, P. M. Ismail, W. Bai, J. J. Yang, L. Yang, H. H. Zhang, M. Cheng, H. Y. Li, Q. Zhang, C. Xiao and Y. Xie, *Adv. Mater.*, 2022, **34**, 2200563.
28 M. Cheng, C. Xiao and Y. Xie, *J. Mater. Chem. A*, 2019, **7**, 19616–19633.
29 N. Cherkasov, A. O. Ibhadon and P. Fitzpatrick, *Chem. Eng. Process.*, 2015, **90**, 24–33.
30 X. Z. Chen, N. Li, Z. Z. Kong, W. J. Ong and X. J. Zhao, *Mater. Horiz.*, 2018, **5**, 9–27.
31 W. J. Ren, Z. W. Mei, S. S. Zheng, S. N. Li, Y. M. Zhu, J. X. Zheng, Y. Lin, H. B. Chen, M. Gu and F. Pan, *Research*, 2020, **2020**, 3750314.
32 Y. T. Wang, Y. F. Yu, R. R. Jia, C. Zhang and B. Zhang, *Natl. Sci. Rev.*, 2019, **6**, 730–738.
33 X. B. Chen, L. Liu, P. Y. Yu and S. S. Mao, *Science*, 2011, **331**, 746–750.
34 H. Tong, S. X. Ouyang, Y. P. Bi, N. Umezawa, M. Oshikiri and J. H. Ye, *Adv. Mater.*, 2012, **24**, 229–251.
35 X. C. Wang, K. Maeda, A. Thomas, K. Takanabe, G. Xin, J. M. Carlsson, K. Domen and M. Antonietti, *Nat. Mater.*, 2009, **8**, 76–80.
36 W. J. Ong, L. L. Tan, Y. H. Ng, S. T. Yong and S. P. Chai, *Chem. Rev.*, 2016, **116**, 7159–7329.
37 R. B. Xu, M. H. Su, Y. H. Liu, Z. B. Chen, C. Ji, M. L. Yang, X. Y. Chang and D. Y. Chen, *J. Cleaner Prod.*, 2020, **242**, 118366.
38 Y. S. Li, M. R. Ti, Z. Q. Li, Y. Zhang, L. Wu and Y. J. He, *J. Mater. Sci.: Mater. Electron.*, 2021, **32**, 2268–2282.
39 T. T. Xiao, Z. Tang, Y. Yang, L. Q. Tang, Y. Zhou and Z. G. Zou, *Appl. Catal., B*, 2018, **220**, 417–428.
40 Y. J. Xue, Y. C. Guo, Z. G. Liang, H. Z. Cui and J. Tian, *J. Colloid Interface Sci.*, 2019, **556**, 206–213.
41 Y. Li, M. Ti, D. Zhao, Y. Zhang, L. Wu and Y. He, *J. Alloys Compd.*, 2021, **870**, 159298.
42 Y. T. Xiao, G. H. Tian, W. Li, Y. Xie, B. J. Jiang, C. G. Tian, D. Y. Zhao and H. G. Fu, *J. Am. Chem. Soc.*, 2019, **141**, 2508–2515.
43 Y. J. Xue, X. K. Kong, Y. C. Guo, Z. Q. Liang, H. Z. Cui and J. Tian, *J. Materiomics*, 2020, **6**, 128–137.
44 X. Chen, J. Y. Li, Z. R. Tang and Y. J. Xu, *Catal. Sci. Technol.*, 2020, **10**, 6098–6110.
45 V. Luxmi and A. Kumar, *Mater. Sci. Semicond. Process.*, 2019, **104**, 104690.
46 S. Prabhu, S. Manikumar, L. Cindrella and O. J. Kwon, *Mater. Sci. Semicond. Process.*, 2018, **74**, 136–146.
47 W. Yu, J. Chen, T. Shang, L. Chen, L. Gu and T. Peng, *Appl. Catal., B*, 2017, **219**, 693–704.
48 J. Meng, X. Wang, Y. Liu, M. Ren, X. Zhang, X. Ding, Y. Guo and Y. Yang, *Chem. Eng. J.*, 2021, **403**, 126354.
49 H. Yu, R. Shi, Y. Zhao, T. Bian, Y. Zhao, C. Zhou, G. I. N. Waterhouse, L. Z. Wu, C. H. Tung and T. Zhang, *Adv. Mater.*, 2017, **29**, 1605148.
50 J. Fu, Q. Xu, J. Low, C. Jiang and J. Yu, *Appl. Catal., B*, 2019, **243**, 556–565.
51 Y. Wang, X. Di, X. Wu and X. Li, *J. Alloys Compd.*, 2020, **846**, 156215.
52 W. Ho, Z. Zhang, W. Lin, S. Huang, X. Zhang, X. Wang and Y. Huang, *ACS Appl. Mater. Interfaces*, 2015, **7**, 5497–5505.
53 Y. Quan, M. Liu, H. Wu, X. Tian, L. Dou and Z. Wang, *Appl. Surf. Sci.*, 2024, **642**, 158601.
54 S. Chen, Y. Hu, S. Meng and X. Fu, *Appl. Catal., B*, 2014, **150**, 564–573.
55 X. Liu, A. Jin, Y. Jia, T. Xia, C. Deng, M. Zhu, C. Chen and X. Chen, *Appl. Surf. Sci.*, 2017, **405**, 359–371.
56 M. Chatterjee, M. Mondal, T. Sukul, K. Ghosh and S. K. Pradhan, *J. Ind. Eng. Chem.*, 2023, **127**, 390–405.
57 S. Zwane, D. S. Dlamini, B. B. Mamba and A. T. Kuvarega, *Inorg. Chem. Commun.*, 2023, **151**, 110637.
58 M. Lv, H. Wang and H. Shi, *Colloids Surf., A*, 2023, **679**, 132579.
59 C. Mrabet, R. Jaballah, N. Mahdhi, A. Boukhachem and M. Amlouk, *J. Alloys Compd.*, 2023, **968**, 172252.
60 K. Li, J. Zhu, W. Zhou, L. Sun and S. Tian, *J. Alloys Compd.*, 2023, **968**, 171955.
61 L. Zhang, J. Qiu, G. Xia, D. Dai, X. Zhong and J. Yao, *J. Mater. Sci. Technol.*, 2023, **138**, 214–220.
62 X. Mo, X. Zhang, B. Lin, C. Ning, M. Li, H. Liao, Z. Chen and X. Wang, *J. Mater. Sci. Technol.*, 2023, **145**, 174–184.